The Astrophysical Journal, 838:45 (12pp), 2017 March 20 https://doi.org/10.3847/1538-4357/aa6347

The 2014 X-Ray Minimum of η Carinae as Seen by *Swift*

M. F. Corcoran[1,2], J. Liburd[3], D. Morris[3], C. M. P. Russell[4], K. Hamaguchi[1,5], T. R. Gull[6], T. I. Madura[7], M. Teodoro[2,6], A. F. J. Moffat[8], N. D. Richardson[9], D. J. Hillier[10], A. Damineli[11], and J. H. Groh[12]
[1] CRESST and X-Ray Astrophysics Laboratory, NASA/Goddard Space Flight Center, Greenbelt, MD 20771, USA
[2] Universities Space Research Association, 7178 Columbia Gateway Drive, Columbia, MD 21044, USA
[3] University of the Virgin Islands, College of Science and Mathematics, #2 John Brewers Bay, St. Thomas, USVI 00802-9990, USA
[4] NASA Goddard Space Flight Center, Code 662, Greenbelt, MD 20771, USA
[5] Department of Physics, University of Maryland, Baltimore County, 1000 Hilltop Circle, Baltimore, MD 21250, USA
[6] NASA Goddard Space Flight Center, Code 667, Greenbelt, MD 20771, USA
[7] Department of Physics and Astronomy, San Jose State University, One Washington Square, San Jose, CA 95192, USA
[8] Département de physique and Centre de Recherche en Astrophysique du Québec (CRAQ), Université de Montréal, C.P. 6128, Succ. Centre-Ville, Montréal, Québec, H3C 3J7, Canada
[9] Ritter Observatory, Department of Physics and Astronomy, The University of Toledo, Toledo, OH 43606, USA
[10] Department of Physics and Astronomy & Pittsburgh Particle Physics, Astrophysics, and Cosmology Center (PITT PACC), University of Pittsburgh, 3941 O'Hara Street, Pittsburgh, PA 15260, USA
[11] Instituto de Astronomia, Geofísica e Ciências Atmosféricas, Universidade de São Paulo, Rua do Matão 1226, Cidade Universitária, São Paulo, 05508-900, Brazil
[12] School of Physics, Trinity College Dublin, Dublin 2, Ireland
Received 2016 December 30; revised 2017 February 22; accepted 2017 February 22; published 2017 March 22

Abstract

We report on *Swift* X-ray Telescope observations of Eta Carinae (η Car), an extremely massive, long-period, highly eccentric binary obtained during the 2014.6 X-ray minimum/periastron passage. These observations show that η Car may have been particularly bright in X-rays going into the X-ray minimum state, while the duration of the 2014 X-ray minimum was intermediate between the extended minima seen in 1998.0 and 2003.5 by *Rossi X-Ray Timing Explorer* (*RXTE*), and the shorter minimum in 2009.0. The hardness ratios derived from the *Swift* observations showed a relatively smooth increase to a peak value occurring 40.5 days after the start of the X-ray minimum, though these observations cannot reliably measure the X-ray hardness during the deepest part of the X-ray minimum when contamination by the "central constant emission" component is significant. By comparing the timings of the *RXTE* and *Swift* observations near the X-ray minima, we derive an updated X-ray period of $P_X = 2023.7 \pm 0.7$ days, in good agreement with periods derived from observations at other wavelengths, and we compare the X-ray changes with variations in the He II 4686 emission. The middle of the "Deep Minimum" interval, as defined by the *Swift* column density variations, is in good agreement with the time of periastron passage derived from the He II λ4686 line variations.

Key words: binaries: general – stars: individual ([HD 93308]eta Carinae) – stars: winds, outflows – stars: early-type – stars: massive – X-rays: stars

Supporting material: machine-readable tables

1. Introduction

For stars, mass is destiny; but for extremely massive stars ($M > 60\,M_\odot$), mass loss (and the accompanying loss of stellar angular momentum) plays an important role in determining that destiny. Mass is lost via radiatively driven stellar winds and large-scale transient eruptions. These eruptions, transient super-Eddington outbursts of indeterminate origin and length, may play an important, perhaps even dominant, role in removing the H-rich stellar envelope (Humphreys & Davidson 1994; Smith & Owocki 2006). It is currently unclear whether these eruptive events, or more stable radiatively driven winds, determine the final mass of the star. This leads to substantial uncertainty in understanding the evolution of extremely massive stars from the main sequence to eventual supernovae, and to neutron stars, magnetars, or black holes.

Eta Carinae (η Car; Davidson & Humphreys 1997; Humphreys & Martin 2012) is the most massive and most luminous binary star system within 3 kpc. It contains a violently eruptive luminous blue variable star, η Car-A ($M_{\rm initial} > 100\,M_\odot$, Hillier et al. 2001). In the interval 1837–1843, the system was observed to suffer a series of extreme brightenings (Herschel 1838), a period called the "Great Eruption" by Davidson & Humphreys (1997). During this event, the system ejected $\gtrsim$10–40 $M_\odot$ (Morris et al. 1999; Smith et al. 2003; Smith 2013; Morris 2015), forming the dusty, bipolar Homunculus Nebula (Gaviola 1950; Steffen et al. 2014) that today surrounds and obscures the star. Shrouded as it is by the Homunculus, direct studies of the star are confoundingly difficult, and for more than a century the nature of the star (and, in fact, whether the star itself still existed—for example, Ostriker & Gunn 1971) was controversial.

The first stage in the modern understanding of η Car was the observation by Westphal & Neugebauer (1969) that the Homunculus was the brightest extra-solar object in the infrared, with $f_{\rm IR} = 2.8 \times 10^{-5}$ erg s^{-1} cm^{-2} in the 0.4–19.5 μ band, corresponding to $L_{\rm IR} \geqslant 4.4 \times 10^6\,L_\odot$ at an assumed distance to η Car of 2300 pc. Davidson (1971) realized this enormous luminosity was probably UV thermal radiation from a hot, superluminous massive star, absorbed and re-radiated by dust in the Homunculus.

Another key step in understanding η Car came in the 1990s with the discovery of a strict 2024 day periodicity at nearly all wavebands (see Damineli et al. 2008a, and references therein), including the X-ray band. The X-ray variability is now recognized to arise from a zone of hot shocked gas produced

by collision of the wind of an extremely luminous, massive, unstable star the wind of a companion star, modulated by orbital motion. The periodic X-ray variability is arguably the most direct indication that the star is a massive, long-period, extremely eccentric ($e \sim 0.9$) binary system consisting of the very massive primary (η Car-A) and a luminous, massive, hotter (but not otherwise directly seen) companion star, η Car-B (Pittard & Corcoran 2002; Verner et al. 2005; Mehner et al. 2010a).

The primary, η Car-A, loses mass at a prodigious rate, $\dot{M} \approx 10^{-3}\,M_{\odot}$ yr^{-1} (Hillier et al. 2001; Groh et al. 2012a), via a radiatively driven stellar wind. This is the largest (quasi-) steady wind-driven mass-loss rate of any star known. The companion star, η Car-B, also possesses a strong, radiatively driven wind, but with a mass-loss rate that is believed to be a factor of ~100 lower than that of η Car-A (Pittard & Corcoran 2002; Groh et al. 2012a). Eta Car's variable 2–10 keV X-ray emission is produced by the strong collision of the thin, fast wind ($V_{\infty} \approx 3000$ km s^{-1}; Pittard & Corcoran 2002) from η Car-B with the massive, slower wind ($V_{\infty} \approx 420$ km s^{-1}; Groh et al. 2012a) of η Car-A. Although η Car-B's wind speed is more than a factor of five larger than the wind speed of η Car-A, the much larger mass-loss rate of η Car-A means that the wind of η Car-A pushes against the wind of η Car-B, forming a bow shock that is closer to and concave around the companion star. Analysis of the orbital phase-locked X-ray variability provides our most direct constraints on the momentum ratio of the two winds, the orbital eccentricity, and the shape of the colliding wind "bow shock" formed around the secondary star. This bow shock produces a low-density cavity in the primary's wind in the primary's wind. This low-density cavity allows ionizing radiation from the secondary and primary to escape and illuminate the circumstellar nebulosity like a lighthouse beacon (e.g., see Madura et al. 2012) and is responsible for producing evolving density and ionization structures seen at distances of hundreds of au from the central star (Gull et al. 2016). This cavity also allows a view into the inner wind of η Car-A when the stars are close to periastron. The illumination of the Homunculus by radiation escaping through the wind cavity produces optical and UV line variations (Groh et al. 2012a, 2012b), correlated (but time-delayed) with the X-ray lightcurve. These UV variations have been used to determine the physical orientation of the system and to map the recent history of its mass loss (see Madura et al. 2012, 2013; Teodoro et al. 2013; however, alternative interpretations of the system orientation have also been explored—for example, Soker & Kashi 2012 and references therein).

As shown by detailed monitoring with the *Rossi X-Ray Timing Explorer* (*RXTE*; Bradt et al. 1993) from 1996 February through 2011 December (Ishibashi et al. 1999; Corcoran et al. 2001; Corcoran 2005; Corcoran et al. 2010), the X-ray emission is characterized by a gradual rise in X-ray brightness, which evolves into rapid, strong X-ray variations, followed by a sudden decrease to a minimum brightness level (Ishibashi et al. 1999; Corcoran & Ishibashi 2012). The start of this minimum state is reproducible to within 1 day over the last 18 years, and has been used to define the 2024 day orbital period. The short duty cycle of the X-ray minimum ($\Delta t/P \approx 4.4\%$) shows that the minimum occurs near periastron passage (when the stars are moving most rapidly), though the exact timing of periastron passage is still somewhat uncertain. Similar X-ray variability is characteristic of the well-established, long-period, eccentric, X-ray emitting colliding wind binary, WR 140 (Williams et al. 1990; Corcoran 2012).

Observed orbit-to-orbit X-ray emission variations in η Car (Corcoran et al. 2010; Corcoran 2012) complicate this rather simple picture. These variations must arise from changes in the stellar wind properties of one or both of the stars. In particular, the duration of the X-ray minimum state, which began in 2009 January, was shorter by about 30 days compared with the two X-ray minima observed previously (Kashi & Soker 2009a; Pian et al. 2009; Corcoran et al. 2010). The cause of this abrupt recovery is controversial; suggestions include significant changes in η Car-A's wind mass-loss rate (by a factor of a few) or variations in wind velocity (Kashi & Soker 2009a; Corcoran et al. 2010) or wind clump properties (Teodoro et al. 2012b). None of these explanations are entirely satisfactory.

The most recent X-ray minimum of the η Car system began in 2014 August. Because of the end of the *RXTE* mission in 2012 January, new observations of η Car with *RXTE* were not possible. Instead, we were able to use the X-Ray Telescope (XRT; Burrows et al. 2005) on the *Swift* observatory (Gehrels et al. 2004) to monitor the 2–10 keV X-ray variation of η Car in 2014. The *Swift* X-ray observations were obtained along with other multi-wavelength observations, which included ground-based spectroscopy from observatories around the world, imaging spectroscopy with the *HST*/STIS, and X-ray spectral imaging with *CHANDRA*, *XMM*, *Suzaku*, and *NuSTAR*. The results of these observations are reported elsewhere (e.g., see Hamaguchi et al. 2014b; Davidson et al. 2015a; Mehner et al. 2015; Gull et al. 2016; Richardson et al. 2016; Teodoro et al. 2016).

We report here the results of the X-ray observations of η Car by the *Swift* XRT in 2014. In Section 2 we discuss the reduction and analysis of the XRT observations. In Section 4 we compare the *Swift* XRT 2–10 keV X-ray lightcurve of η Car, augmented with data obtained by *RXTE* after those reported by Corcoran et al. (2010), and compare these data to recalibrated *RXTE* X-ray flux measures from 1996 to 2011. We discuss refinement of the X-ray period using the *Swift* and *RXTE* data in Section 4.2. In Section 4.3 we compare the hardness ratio (HR) variations from *RXTE* and *Swift* around X-ray minimum, and compare column density variations seen by *Swift* with those seen by *CHANDRA* and *XMM* in 2003 (Hamaguchi et al. 2007a, 2014). We summarize the results of the X-ray monitoring in Section 5.

2. *Swift* Observations

The most recent X-ray observations of η Car by *Swift* began in 2014 April. Observations were scheduled twice per week at the outset; however, as things developed, we were allocated more frequent monitoring at the *Swift* director's discretion. These observations (including alternate-day observations near the start and end of the X-ray minimum) were critical to sample the X-ray behavior when the X-ray state was changing most rapidly. The *Swift* log of the 2014 observations discussed here is given in Table 1. For our discussion, we also include recalibrated fluxes from *RXTE*, including previously unpublished observations from 2010 through 2011.

2.1. Swift *Observing Mode*

For optically bright sources like η Car, there is a finite probability that optical photons can penetrate the blocking filter of the *Swift* XRT and be misregistered as X-ray photon events by the on-board electronics, a phenomenon called "optical loading."[13] For the past decade, η Car has been increasing in optical brightness (Martin et al. 2006b; Fernández-Lajús et al. 2009), partially due to clearing out of circumstellar dust along the line of site, with possible contributions from an intrinsic increase in stellar luminosity (Davidson et al. 1999). At the time of the *Swift* 2014 observations, optical monitoring at the La Plata Observatory[14] showed that η Car increased in brightness from $V = 4.45$ to 4.25, and thus, at these magnitudes, optical loading is a concern. To mitigate optical contamination, we used windowed timing (WT) mode[15] rather than photon counting mode for the XRT observations. In WT mode, 10 CCD rows at a time are accumulated in the serial register, and only the central 200 columns ($\sim 8'$) of the field of view are read out, using a readout time of 1.7 ms. Use of WT mode reduces the biasing of the data due to optical loading to a negligible level at the expense of spatial information in one direction. The observed η Car XRT rate was $\lesssim$2.5 cts s^{-1}, so that photon pile-up (in which two or more lower-energy photons are misregistered as a single higher-energy photon) is not a concern (pile-up is only important for rates greater than $\sim$100 cts s^{-1} in WT mode).

2.2. Data Reduction and Analysis

The location of η Car recorded in the FITS file headers in observations originally produced by the *Swift* standard processing software before version 3.16.04 was incorrect, so that the derived X-ray position of η Car was offset from its known position in the WT-mode images. We re-registered these data spatially using the `xrtpipeline` processing software with the sky coordinates of η Car specified directly. In all the observations (even during the X-ray minimum), η Car was the brightest source in the collapsed WT image. We extracted source photons from a region of $1'$ in the spatial direction of the 1D image. We extracted background counts from apparently source-free regions in each 1D WT image, again using a $1'$ extraction region in the spatial direction in order to determine net, background-subtracted source spectra.

We extracted data in the energy range 0.3–10.0 keV, and spectra were binned to a minimum of 10 counts per bin before subtracting the background. The binned net source spectra were fit using XSPEC version 12.8 or higher (Dorman & Arnaud 2001), with a photoelectrically absorbed, two-temperature model based on the ATOMDB atomic data and spectral models output from the Astrophysical Plasma Emission Code (Smith et al. 2001; Foster et al. 2012) to represent the collisionally ionized diffuse gas. We also included a Gaussian emission line to represent the known Fe fluorescence line at 6.4 keV (Corcoran et al. 2000). This model is consistent with analysis of higher-resolution, higher signal-to-noise X-ray observations of η Car, and provided a statistically acceptable fit to the XRT spectra. We also included a low-energy component to account for soft flux in the source aperture due to spatially variable extended emission in the Carina nebula (Hamaguchi et al. 2007b; Townsley et al. 2011) and any residual emission due to leakage of optical photons. We fit the net counts with this model using effective areas calculated individually for each observation, including the appropriate spectral response matrix from version 20140614 of the *Swift*/XRT calibration database. We calculated fluxes from the net spectra using the XSPEC "`flux`" command in the 2.0–10.0 keV band and calculated column densities using the Wisconsin photoelectric absorption model (`wabs`). We noted that for five observations in which the source was placed near bad or hot pixels on the detector, the derived flux was especially sensitive to the exact location of the extraction region, which could cause an additional systematic uncertainty in the derived flux of $\sim$20%–30%. For these observations, we adjusted the source extraction region, remeasured the fluxes independently, and averaged the data points as an estimate of the systematic uncertainty.

2.3. Contamination from Neighboring Sources

Because η Car resides in the Carina Nebula, an area rich in X-ray sources (see, for example, Townsley et al. 2011), and because the collapsed WT image only preserves spatial information in one-dimension, other sources included in the collapsed image of η Car could contribute to the extracted source and/or background data. Sources included in our adopted WT source extraction region would artificially make η Car appear brighter in X-rays; conversely, a source included in the adopted background region could artificially increase the extracted background flux, making the net flux from η Car appear too low. In addition, because the WT-mode data were not all obtained at the same spacecraft roll angles, different contaminating sources could be included in the compressed WT-mode data obtained at different roll angles. The overall effect of this could be to introduce spurious variability at some level in the derived source fluxes. Cross-calibration of the *Swift* X-ray fluxes with better spatially resolved measures obtained by *CHANDRA*, *XMM*, *Suzaku*, and *NuSTAR* (Hamaguchi et al. 2016) near the times of the *Swift* observations generally showed good agreement. We further investigated the contribution of neighboring sources in the compressed WT source and background regions in the following way. For each *Swift* XRT-WT observation, we used the *Swift* XRT exposure map (which shows the exposure time of the full 2D region of the XRT for the spacecraft roll angle) to determine the 2D region of the field that is included in the compressed, 1D WT observation. We then masked the region appropriate to this exposure map in a suitable *XMM* image of the Carina Nebula (the MOS2 image from observation ID 0560580101, PI Hamaguchi, observation date 2009 January 05, $\phi = 1.994$) to determine which X-ray sources are included in the *Swift* XRT-WT observation. Figure 1 gives an overview of this process. We then extracted the total number of counts in the 2–10 keV energy range from the *XMM* masked image for our adopted WT-mode source and background regions, and converted these rates to equivalent *Swift* XRT rates using the Portable, Interactive Multi-mission Simulator[16] (PIMMS), assuming an absorbed thermal optically thin emission model with $N_{\rm H} = 2 \times 10^{21}$ cm^{-2}

[13] http://www.swift.ac.uk/analysis/xrt/optical_loading.php
[14] http://etacar.fcaglp.unlp.edu.ar/
[15] http://www.swift.ac.uk/analysis/xrt/modes.php
[16] http://heasarc.gsfc.nasa.gov/docs/software/tools/pimms.html

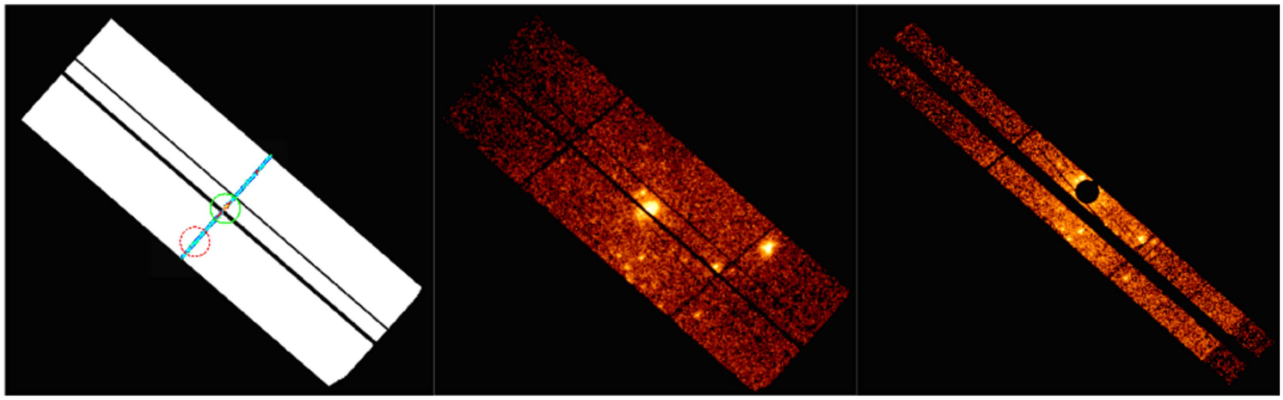

Figure 1. Method for estimating the neighboring source contribution to the adopted source and background regions for a representative *Swift* XRT-WT observation. Left: the tilted white area shows the region of the *Swift* XRT exposure map for the specific spacecraft roll angle, which shows the full region that is included in the 1D WT image. The dark lines running from the upper left to lower right in the exposure map are bad detector CCD columns that have no useful exposure. The blue line running across the exposure map is the 1D WT-mode image from this observation. Circles of radius 1′ around η Car and around the adopted background region are shown in green and red, respectively. Middle: an image of the Carinae Nebula obtained by XMM-Newton and masked to correspond to the *Swift* XRT exposure map. Right: the upper strip shows the region of the Carina Nebula that is included in the adopted source region for this WT observation. The dark region is a 1′ circle that masks out η Car. The lower strip shows the region of the Carina Nebula included in the adopted background region. For all images, north is to the top, and east is to the left.

Table 1
Swift X-Ray Telescope Observations

Sequence	Date	MJD	Δt (d)	ϕ	Expo. (s)	Flux (10^{-10} erg s^{-1} cm^{-2})	HR[a]	$N_{\rm H}$ (10^{22} cm^{-2})
91911002	2014 Apr 05	56752.7300	0.018	2.942	1517.0	1.71 ± 0.08	−0.70 ± 0.02	$4.72^{+9.72}_{-0.92}$
91911003	2014 Apr 09	56756.3306	0.016	2.944	1406.0	1.77 ± 0.10	−0.76 ± 0.02	$3.30^{+1.36}_{-0.63}$
91911004	2014 Apr 12	56759.5272	0.016	2.945	1412.0	1.40 ± 0.09	−0.73 ± 0.03	$3.16^{+5.17}_{-0.12}$
91911005	2014 Apr 16	56763.4583	0.017	2.947	1434.0	1.18 ± 0.37	−0.67 ± 0.03	$6.07^{+2.30}_{-1.80}$
91911006	2014 Apr 19	56766.4666	0.017	2.949	1435.0	1.15 ± 0.09	−0.73 ± 0.03	$3.66^{+0.86}_{-0.47}$
91911007	2014 Apr 23	56770.7309	0.017	2.951	1457.0	1.54 ± 0.33	−0.62 ± 0.03	$11.16^{+5.15}_{-3.67}$
91911008	2014 Apr 26	56773.3205	0.017	2.952	1460.0	1.45 ± 0.08	−0.68 ± 0.03	$8.67^{+7.17}_{-2.45}$

Note.
[a] Hardness ratios calculated according to Equation (1).
(This table is available in its entirety in machine-readable form.)

(appropriate for the interstellar column to the Carina Nebula) with $kT = 0.5$ keV. We then compared the resulting rates to the net count rates we derived from the XRT-WT observations. We found that the typical contribution to the derived net count rates due to the neighboring sources included in the source and background regions in the WT-mode observations is approximately 0.1 counts s^{-1} for all the *Swift* observations. This is $\lesssim$10% for most of the observations. However, during the X-ray minimum, the neighboring sources contribute an amount that is comparable to the net rate we derived from our WT analysis, which means that absolute fluxes during the X-ray minimum should be treated with caution. The observation-to-observation variation produced by variations in the cosmic background with varying roll angle is much lower, so that relative changes in flux and spectra over the entire *Swift* data set are much better determined.

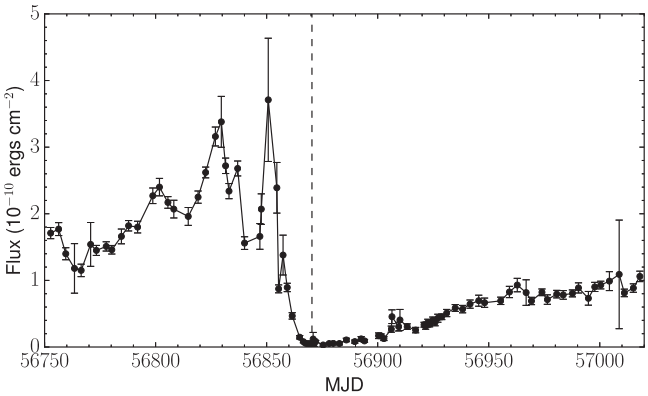

Figure 2. *Swift* XRT 2–10 keV X-ray lightcurve of η Car, from 2014 April to 2014 December. Fluxes are not corrected for absorption. The maximum brightness occurred on 2014 July 12 (MJD 56850), and the X-ray minimum began on 2014 August 1 (MJD 56870.0), as indicated by the dashed vertical line.

3. Flux and Color Variations

3.1. Flux Variations

Figure 2 shows the derived *Swift* XRT X-ray fluxes of η Car (not corrected for intervening absorption) from 2014 April through 2014 December (see Table 1). The X-ray emission prior to the decline to the minimum state showed three strong peaks, similar to the flaring behavior seen

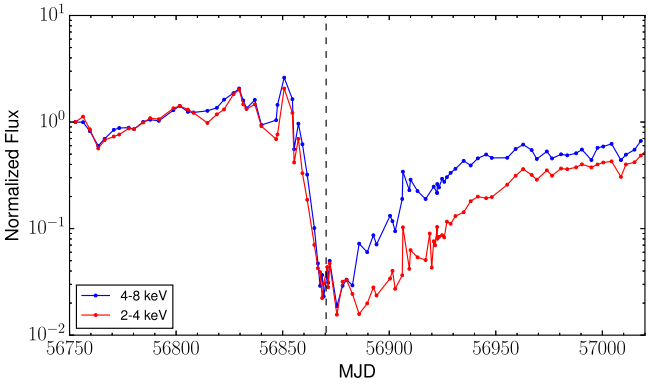

Figure 3. Observed *Swift* XRT 4–8 keV X-ray flux compared to that in the 2–4 keV band. Fluxes are not corrected for absorption but have been normalized to the flux level for the first observation in each band. The vertical line marks the start of the X-ray minimum.

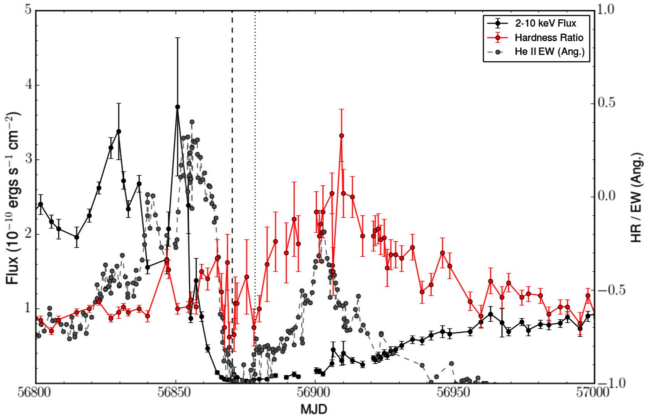

Figure 4. Plot of the X-ray hardness (in red), as defined previously, compared with X-ray flux (black) near the 2014 X-ray minimum. Note that there is no obvious change in hardness during the X-ray "flare" peaks prior to the X-ray minimum state. The black vertical dashed line marks the start of the X-ray minimum. The dotted line marks the end of the interval of low hardness after the start of the minimum, which we interpret as the end of the "Deep X-Ray Minimum" state. The gray dots are the unbinned He II λ4686 emission equivalent widths (in Å) from Teodoro et al. (2016). Both the hardness ratio and the He II emission equivalent widths are plotted against the right y-axis.

in previous cycles (Corcoran et al. 1997; Moffat & Corcoran 2009), superimposed on an overall X-ray brightening. Points outside the X-ray minimum state with large error bars are those in which the source was affected by bad or hot detector pixels (which have larger systematic errors, as discussed previously). These data have not been corrected for nearby sources that may have contaminated the source and/or background spectra as described previously, so that there may be an additional uncertainty in the derived absolute fluxes of ~10%.

The maximum flux observed to date was $3.71 \pm 0.93 \times 10^{-10}$ erg s^{-1} cm^{-2} in the 2–10 keV band (corresponding to a luminosity of 2.35×10^{35} erg s^{-1} for an assumed distance of 2.3 kpc) observed on 2014 July 12 (MJD 56850.7). This is the brightest that η Car has been in more than 18 years of X-ray observations by *RXTE*, *Swift*, or any imaging X-ray observatory, and 27% brighter than the previous observed maximum (2.79×10^{-10} erg s^{-1} cm^{-2}, which was observed on 2008 December 6 by *RXTE*). The *Swift* XRT peak flux is a factor of 1.5 lower than the 2–10 keV flux peak reported by the non-imaging *MAXI* instrument on 2014 June 17 (Negoro et al. 2014), which was 0.07 photons cm^{-2} s^{-1}, equivalent to an energy flux of 5.2×10^{-10} erg s^{-1} cm^{-2} using our spectral model. However, *Swift* XRT observations on June 14 and 18 were 2.62 ± 0.07 and $3.18 \pm 0.1 \times 10^{-10}$ erg s^{-1} cm^{-2}, respectively, significantly lower than the reported *MAXI* flux. This could mean that the *MAXI* flux on June 17 was overestimated, or that the flaring timescale was dramatically shorter near the time of the *MAXI* observation.

3.2. X-Ray Color Changes

Hamaguchi et al. (2014a) reported significant differences between the time variability of the "hard-band" ($4 < E < 8$ keV) X-ray flux from the central point source in the η Car system and the soft $2 < E < 4$ keV band, using *CHANDRA*, *Suzaku*, and *XMM* spectra (and an individual *Swift* observation) obtained before and during the η Car X-ray minimum in 2009. They specifically noted that in the 4–8 keV band, the decline to X-ray minimum apparently started earlier was steeper, and the minimum level was reached sooner than in the 2–4 keV band (see Figure 2 in Hamaguchi et al. 2014a). For comparison, we extracted data in similar soft (2–4 keV, red) and hard (4–8 keV, blue) bands from our 2014 *Swift* XRT observations. Figure 3 compares the variation of the normalized 2–4 keV band (in blue) with that of the 4–8 keV band, where the fluxes have been normalized simply by dividing by the flux in the first observation in each band. In the soft band, which is more sensitive to absorption, the decline to minimum starts by about MJD 56840 (=2014-07-02), which is earlier than the apparent decline in the hard band. This suggests that prior to the minimum, the soft-band flux is more strongly influenced by wind absorption than the hard-band flux, and that the hottest region of the shock is not more strongly absorbed by the wind from η Car-A than the soft-band flux. The hard-band flux and the soft-band flux both reach their minimum state nearly simultaneously. Near the start of the X-ray minimum, the normalized hard-band flux is about the same, or even lower, than the normalized flux in the soft band, which probably indicates that in this narrow phase, interval emission is dominated by the "Central Constant Component," which is probably not directly associated with the wind–wind collision. The hard-band flux begins to recover before the soft-band flux, since the optical depth to the hot shocked colliding wind region through the wind of η Car-A is higher in the soft band than the hard band.

Changes in X-ray absorption are of interest, since they provide a measure of the amount of η Car-A's wind that lies in front of the X-ray source and can be used to constrain the density profile of the star's wind. Because of the poor spectral resolution of the Proportional Counter Array (PCA), and lack of response to photons with $E \lesssim 3$ keV, direct fitting of the *RXTE* spectra provided only poor constraints on the absorbing column density. Therefore Corcoran et al. (2010) calculated a HR for the PCA data defined as

$$\mathrm{HR} = (C_7 - C_3)/(C_7 + C_3), \quad (1)$$

where C_7 and C_3 are the gross counts in the 7 ± 0.5 and 3 ± 0.5 keV bands, respectively. This HR serves as a proxy for

changes in absorption (as long as the temperature of the X-ray emitting gas remains roughly constant). Similarly, we calculated the same HR from the *Swift* counts in these same bands (Table 1). Figure 4 compares the *Swift* HRs to the *Swift* fluxes. There is apparently no strong temporal correlation between any flux peak before the X-ray minimum and peaks in spectral hardness. The *Swift* HRs show a gradual rise after the start of the X-ray minimum, reaching a peak near MJD = 56910 and then declining. They also show an abrupt drop starting near MJD = 56870, lasting for about 8 days; this phase interval corresponds to the "Deep X-Ray Minimum" phase (Hamaguchi et al. 2007a, 2014a), during which the X-ray emission from the colliding wind source falls below the X-ray emission of the "Central Constant Emission" component, a quasi-stable, relatively soft source located within 1″ of η Car (Hamaguchi et al. 2014a). The HR variability as seen by *Swift* can be compared with the PCA HR variations shown in Figure 5 of Corcoran et al. (2010). There are obvious instrumental differences between the *Swift* colors and the *RXTE* color curve shown in Corcoran et al. (2010), mostly due to differences in soft X-ray sensitivity (which dominates the differences between the HR measures from the *RXTE* and *Swift* observations away from the minimum) and differences in the cosmic soft X-ray background included in the observations (which dominates the proportional counter unit [PCU]-2 hardness measures from the start of the X-ray minimum up to about $\Delta\phi \approx +0.05 \approx 100$ days afterward).

The *Swift* HR variations of η Car shown in Figure 4 can also be compared to the *RXTE* HRs of WR 140 shown in Figure 3 of Corcoran et al. (2011). WR 140 is a well-established massive binary, and like η Car, it has a long-period and exceptionally high eccentricity and is a strong, variable X-ray source. WR 140 resides in a much more isolated region of the sky than η Car, and it remains sufficiently bright, even during its X-ray minimum state, to allow reliable measures of the X-ray colors by *RXTE*. The WR 140 HRs show a smooth, symmetric rise to a peak hardness, followed by a smooth decline afterward. This variability is similar to that of η Car as seen by *Swift*. WR 140's orbit is precisely determined from a combination of ground-based radial velocity measures (Fahed et al. 2011) and optical interferometry (Monnier et al. 2011), so that the maximum of WR 140's HR is known to occur at inferior conjunction of the Wolf–Rayet component, when the X-ray emitting colliding wind bow shock is maximally hidden behind the thick wind of the Wolf–Rayet star. By analogy, this similarly may suggest that inferior conjunction of η Car-A occurs near the peak hardness seen by *Swift*, 40.5 days after the start of the X-ray minimum. However, observations at higher X-ray energies by Hamaguchi et al. (2016) provide strong evidence that the actual column density peak occurs near the "Deep X-Ray Minimum," suggesting that this time is the actual time of occultation.

3.3. Comparison with He II λ4686

The He II λ4686 emission line, first identified by Steiner & Damineli (2004), and subsequently studied by Martin et al. (2006a), Soker & Behar (2006), Teodoro et al. (2012a), Davidson et al. (2015b), and most completely by Teodoro et al. (2016), is also seen to vary in strength with the binary orbit. Figure 4 compares the X-ray broad-band flux and HR variations from the 2014 minimum seen by *Swift* with the full set of observations of the He II λ4686 emission line equivalent widths from Teodoro et al. (2016). The X-ray flux and He II equivalent widths show similar behavior in that both increase prior to MJD 56850 (=2014-07-12). At this time, the X-ray flux begins to decline, while the observed decline in the He II emission line strength begins about 10 days later. The decline of the He II emission line is more precipitous than that of the X-ray flux, but both reach a minimum at nearly the same time. In addition, during the X-ray "Deep Minimum" interval bounded by the dashed and dotted lines in Figure 4, the He II λ4686 emission line disappears, reappearing at the end of the "Deep Minimum" interval. As discussed by Martin et al. (2006a), Madura et al. (2013), and Teodoro et al. (2016), the He II emission near periastron is believed to be produced close to the WWC region, ionized by some combination of the stellar UV radiation from the hot inner wind of η Car-A, the UV photospheric flux of η Car-B, with perhaps a contribution from the soft X-ray emission near the wind–wind collision boundary (Soker & Behar 2006). Teodoro et al. (2016) argued that the He II variations suggest that periastron passage occurred on MJD 56873.9 (2014-08-04), which is 2.6 days after the start of the Deep X-Ray Minimum, and 1.4 days prior to the center of this interval (MJD 56875.3, 2014-08-06).

Teodoro et al. (2016) have also identified three peaks in the He II λ4686 emission equivalent widths that were coincident in phase with peaks observed during the 2009 periastron passage (Teodoro et al. 2012b). The first two of these peaks occur prior to the X-ray minimum, and in 2014 occurred just after peaks seen in the 2–10 keV X-ray flux. The third peak (Davidson et al. 2015b; Teodoro et al. 2016) occurs during the X-ray minimum, and in 2014 was not obviously associated with any strong change in X-ray flux (though it did occur just prior to a peak in the X-ray HR, as shown in Figure 4).

4. Comparison with Previous X-Ray Observations

4.1. X-Ray Flux Cross-calibration

To study both orbit-dependent and non-orbit-dependent (secular) variations, we include here data obtained by the *RXTE*-PCA in the interval 1996 February 9 through 2011 December 28. Data in the interval 1996 February 9 through 2009 July 30 inclusive have already been discussed elsewhere (Corcoran et al. 2010) but are included here for purposes of comparison. Data extraction and instrumental background correction are as described in Corcoran et al. (2010). Though most of the early *RXTE* data were obtained using 3 PCUs, more recent *RXTE* data were mostly obtained using only 2 PCUs, and only 1 PCU, PCU-2, observed the star from the start to the end of the *RXTE* mission. Therefore, here we only consider the PCU-2 data as the most complete and best-calibrated data.

Corcoran (2005) used a linear scaling based on fluxes derived from contemporaneous *ASCA*, *CHANDRA*, and *XMM* to convert the *RXTE* count rates to net fluxes in the 2–10 keV band. Comparing fluxes derived using this linear scaling to fluxes from direct fitting of the spectrum with an appropriate thermal emission model showed good agreement for earlier data sets, but starting in 2004, there was an increasing discrepancy between the fluxes derived using these two

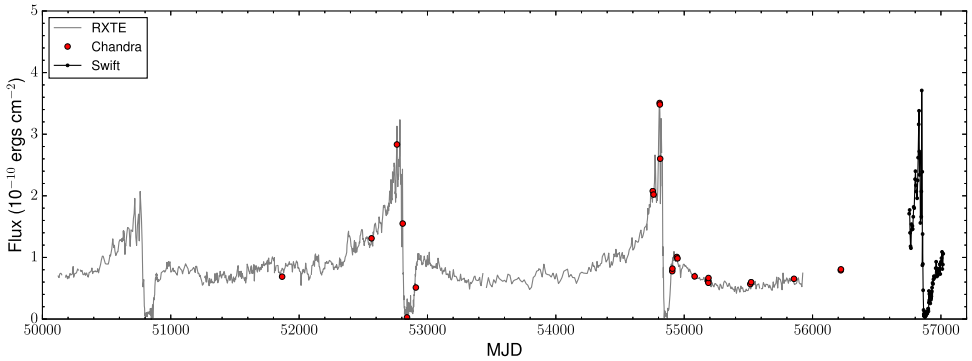

Figure 5. X-ray lightcurve of η Car from 1996 though 2014, in the 2–10 keV band, including data from *RXTE*, *CHANDRA*, and *Swift*. Individual observations from the *CHANDRA* High Energy Transmission Grating and the Advanced CCD Imaging Spectrometer, *Suzaku*, and *XMM* have been used to calibrate the *RXTE* and *Swift* fluxes.

Table 2
Log of *RXTE* Observations and Corrected Fluxes

Sequence	MJD	Δt (d)	ϕ	Expo. (s)	Flux (10^{-10} erg s^{-1} cm^{-2})	Corrected Flux[a] (10^{-10} erg s^{-1} cm^{-2})	Net Rate (s^{-1})	Background Rate (s^{-1})
1996020915	50122.652	0.013	−0.334	1088	0.97 ± 0.02	0.70	11.32 ± 0.18	12.81
1996021610	50129.441	0.011	−0.331	928	0.95 ± 0.02	0.67	10.90 ± 0.20	12.83
1996022113	50134.584	0.012	−0.329	992	1.00 ± 0.02	0.73	11.33 ± 0.19	12.36
1996022920	50142.865	0.011	−0.324	944	1.01 ± 0.02	0.74	10.98 ± 0.20	12.78
1996030520	50147.840	0.011	−0.322	592	1.00 ± 0.02	0.73	10.96 ± 0.24	12.24
1996030814	50150.595	0.009	−0.321	336	0.99 ± 0.03	0.72	10.80 ± 0.35	14.86
1996040704	50180.209	0.011	−0.306	912	0.95 ± 0.02	0.68	10.80 ± 0.20	13.14
1996041216	50185.697	0.012	−0.303	992	0.99 ± 0.02	0.71	11.63 ± 0.22	17.49
1996042217	50195.738	0.013	−0.298	1120	0.93 ± 0.02	0.65	10.11 ± 0.18	13.78
1996042615	50199.671	0.011	−0.296	992	0.97 ± 0.02	0.70	10.26 ± 0.19	13.47

Note.
[a] Flux corrected according to Equation (2).
(This table is available in its entirety in machine-readable form.)

methods. This probably is due to a change in sensitivity of the PCA near this time that is not accounted for properly in the simple linear scaling.

We therefore re-reduced the entire *RXTE* data set in a consistent way. We first defined a simple two-temperature thermal model in which independent X-ray absorption was used for each component. This model adequately fit all the η Car spectra obtained by the *CHANDRA* High Energy Transmission Grating Spectrometer (HETGS) and *Swift*. We then used this model as a template to fit the *RXTE* PCU-2 spectra, holding the temperatures fixed, but allowing the absorption and emission measure of each component to vary. Before fitting, we calculated individual responses for each observation using the software tool `pcarsp`,[17] and estimated particle background for each observation using the `pcabackest (see footnote 17)` routine (both provided by the High Energy Astrophysics Science Archive Research Center). We then calculated model fluxes in the 2–10 keV band from the spectral fit for each observation. These fluxes take into account differences in the *RXTE* response, but need to be calibrated against other data to get absolute source fluxes, since the large field of view of each PCU includes substantial cosmic X-ray background (from both point sources and diffuse emission in the PCU field of view), which is not included in the *Swift* XRT or other imaging X-ray observations. We therefore cross-calibrated the *RXTE* fluxes using fluxes derived by fitting contemporaneous HETGS spectra with the template model. This cross-calibration yields a simple linear fit that accounts for differences between the effective areas of the PCU-2 and the HETGS, as well as differences in the amount of cosmic X-ray sky background included in the derived spectra. The calibrated *RXTE* flux is given by

$$\text{Corr. } RXTE \text{ Flux} = (\text{derived } RXTE \text{ flux} - 0.314)/0.939, \quad (2)$$

where the "derived *RXTE* flux" is the flux derived via fitting the *RXTE* net spectra with our template two-temperature thermal model, and fluxes are given in 10^{-10} erg s^{-1} cm^{-2}. The derived RXTE fluxes are given in Table 2. We then compared the calibrated *RXTE* fluxes derived from contemporaneous spectra obtained by *Swift*, *Suzaku*, Chandra, and *XMM*. There was good agreement between the calibrated *RXTE* fluxes and the fluxes derived from analysis of these other spectra, to within known instrumental cross-calibration uncertainties.

[17] https://heasarc.gsfc.nasa.gov/lheasoft/ftools/xte.html

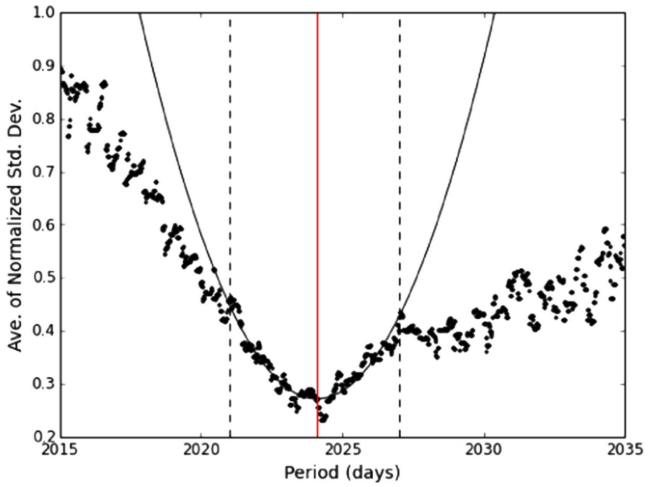

Figure 6. Determination of the X-ray period based on all four X-ray minima monitored by *RXTE* and *Swift* using a binned phase-dispersion minimization of the normalized deviations. The dots show the normalized standard deviations averaged over each phase bin for each test period. The black curve shows the best fit parabola between the limits given by the dashed black lines. The red vertical line is the best fit period, $P = 2024.11$ days.

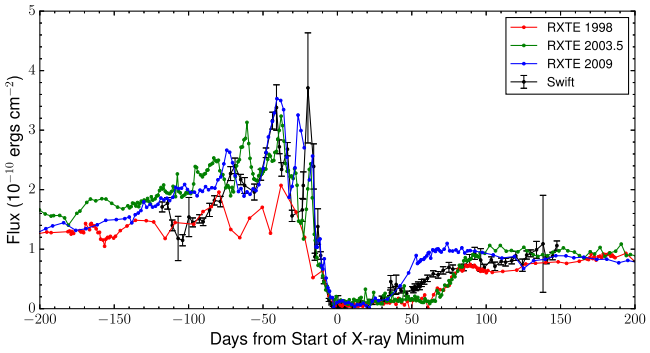

Figure 7. 2–10 keV X-ray lightcurve of η Car near the X-ray minima, compared with the *RXTE* PCU-2 fluxes, using the X-ray ephemeris in Equation (4).

Figure 5 shows the *Swift* XRT lightcurve in the context of the *RXTE* monitoring campaign (including the *CHANDRA* HETGS fluxes). Because *RXTE* was decommissioned on 2012 January 05 (MJD 55566.0), there is a gap in monitoring coverage of η Car from the last *RXTE* observation on 2011 December 28 (MJD 55923.0), until a new monitoring program was begun with *Swift* on 2012 April 03 (MJD 56020.7). While the overall behavior of the X-ray lightcurve is similar from orbit to orbit, and the time when the X-ray minimum level is reached seems strictly reproducible, there are significant differences in the four X-ray cycles sampled so far. In particular, the peak X-ray brightness of η Car just prior to the start of the X-ray minimum seems to be increasing each cycle, while the flux levels away from the X-ray minima seem very similar in all cycles (with perhaps modest variations).

4.2. The X-Ray Period

We used the combined *RXTE* and *Swift* X-ray minima to help refine the X-ray period, using a modified binned phase-dispersion minimization technique (see, for example, Stellingwerf 1978). We chose a set of test periods in the range of 2015–2035 days, and for each test period, we calculated the phased lightcurve. For each phase bin in the phased lightcurve, we then calculated the average flux and the standard deviation of the flux, and normalized the calculated standard deviation in each phase bin by dividing by the average flux in the bin. For each test period, we then calculated the average of all the normalized deviations. To reduce spurious effects due to cycle-to-cycle changes, especially during the strong flaring state near the X-ray maximum, we only considered times within about ± 15 days of the apparent start of the X-ray minimum. Figure 6 shows the normalized standard deviations averaged over each phase bin for each test period. To determine the period that minimizes the deviation, we fit a Gaussian to the deviations, with the fit restricted to the period interval shown by the dashed lines in the figure. The period that minimizes the phase-averaged scatter in the X-ray data is $P_1 = 2024.11$ days.

To further test the robustness of the period determination and get an approximation of the statistical and systematic errors, we also performed an analysis using the Plavchan periodogram, an implementation of binless phase-dispersion minimization (Plavchan et al. 2008), as provided by the NASA Exoplanet Archive.[18] We again restricted the period search to ± 15 days around the apparent start of the X-ray minimum, and we re-normalized the X-ray flux in each of the four X-ray cycles by the maximum of the observed flux. We then fit the resulting PDM power spectrum with a Gaussian to determine the value of the period. The period so determined was $P_2 = 2022.69$ days.

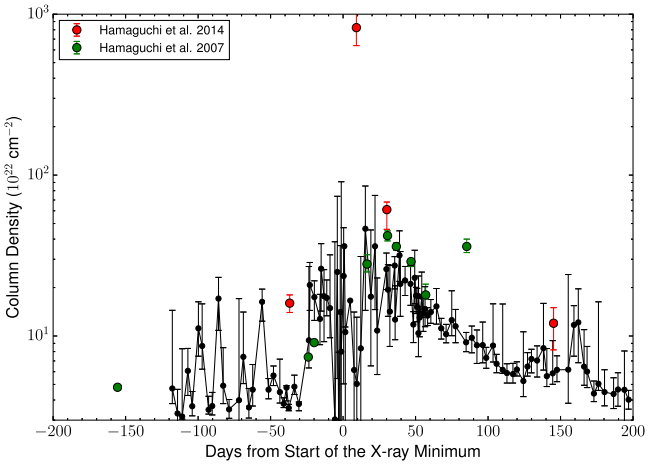

Figure 8. Comparison of column densities derived from fitting the *Swift* XRT spectra and those derived from *XMM* and *CHANDRA* spectra obtained in 2003 (Hamaguchi et al. 2007a), according to the ephemeris given in Equation (4). We also show the *Suzaku* columns from Table 3 in (Hamaguchi et al. 2014b), obtained near the 2009 X-ray minimum. During the "Deep Minimum," the *Swift* X-ray spectrum is dominated by the central constant emission component (Hamaguchi et al. 2007a) as well as more extended emission, so that the column to the colliding wind X-ray source derived from the *Swift* analysis is underestimated during this interval.

[18] http://exoplanetarchive.ipac.caltech.edu/cgi-bin/Periodogram/nph-simpleupload

We adopt the mean of two analyses,

$$P_{\rm X} = 2023.40 \pm 0.71, \quad (3)$$

as the X-ray period, where the quoted error is simply half the difference between the periods found by the two methods. Figure 7 shows the X-ray fluxes from the four observed minima, phased with the following ephemeris:

$$\text{JD (X-ray Min.)} = 2{,}450{,}799.92 + 2023.4E, \quad (4)$$

where E is the cycle count. The X-ray period we derive here agrees well with the period determined from the variation in the equivalent width of the He II λ4686 line, $P_{\rm He} = 2022.7 \pm 0.3$ (Teodoro et al. 2016), and also with the period derived by Damineli et al. (2008b), 2022.7 $\pm$ 1.3 from their joint analysis of optical and X-ray variations. In the remainder of this paper, phases (ϕ) are calculated using the ephemeris given in Equation (4). We note that $\phi = 0$ corresponds well to the start of the "Deep X-Ray Minimum" (Hamaguchi et al. 2007a, 2014a).

Figure 7 compares the three X-ray minima seen by *RXTE* and the 2014 minimum seen by *Swift*. While the first two minima observed by *RXTE* (in 1998.0 and in 2003.5) were of similar durations (≈90 days), the duration of the 2009.0 minimum seen by *RXTE* was only about 60 days. Interestingly, the *Swift* observations of the 2014.6 minimum show that the recovery from the minimum state began at about the same X-ray phase as in 2009.0; however, the X-ray flux then dropped to an intermediate level, lower than the flux at comparable phases in 2009 but brighter than the flux seen in 2003.5 and 1998.0 at those phases. Full recovery from the 2014 X-ray minimum did not occur until $\Delta\phi \approx 0.04$ (i.e., 81 days after the start of the X-ray minimum). Thus the recovery from the 2014 X-ray minimum was intermediate between the abrupt recovery of 2009 and the gradual recoveries of 2003 and 1998.

4.3. Column Density Variations

Column densities derived by fitting spectra from X-ray imaging observatories like *CHANDRA*, *XMM*, and *Suzaku* provide a better measure of the phase at which the maximum hardness (and maximum absorption) occurs for the colliding wind emission from η Car, and thus provide a stringent constraint on the phasing of inferior conjunction of the primary star. To explore the variation in column density near the X-ray minimum, we compare column densities derived from fitting the *Swift* XRT spectra (which have the best time sampling but largest errors) to those derived from fitting *XMM*, *CHANDRA*, and *Suzaku* X-ray spectra (which have higher precision but limited time sampling). Figure 8 compares the absorbing columns derived from analysis of *CHANDRA*, *XMM*, and *Suzaku* spectra (Hamaguchi et al. 2007a, 2014b) obtained during the 2003 and 2009 X-ray minima, with the columns derived from analysis of the 2014 *Swift* XRT spectra. Overall the columns at similar phases are in reasonably good agreement. In general, both the 2014 data and the earlier data show a gradual rise in column from a value of $N_{\rm H} \approx 5 \times 10^{22}$ cm^{-2}, declining after the end of the X-ray minimum, finally reaching the minimum column value just after $\Delta\phi \approx 0.05$ (i.e., 101 days after the start of the X-ray minimum).

There are some noticeable differences in column densities near the "Deep Minimum" and at other phases. Hamaguchi et al. (2014b) derived a column density $82.5^{+43.3}_{-18.7} \times 10^{23}$ cm^{-2} using a *Suzaku*-XIS spectrum from 2009 January 25 ($\phi = 2.005$), during the 2009.0 "Deep Minimum" state. This is the highest column that has yet to be reliably measured. This could indicate a transient excess absorption seen in 2009, which was not observed in 2014. However, as noted previously, when the colliding wind X-ray emission falls to a level comparable to the background in the *Swift* XRT source extraction region, the colors and column densities derived from analysis of the *Swift* XRT spectra become systematically underestimated. This mostly affects observations during the "Deep Minimum," when the colliding wind X-ray source is at its faintest. It seems more probable, therefore, that the extreme column density derived from the *Suzaku*-XIS spectrum from 2009 January 25 is a better measure of the true column to the wind–wind collision at this phase. If so, this means that inferior conjunction of η Car-A occurred near this column density maximum, when the colliding wind X-ray source is hidden behind the bulk of the wind of η Car-A. We suggest that the most recent inferior conjunction of η Car-A occurred close to the midpoint of the "Deep Minimum" interval as seen by *Swift* (i.e., MJD 56875.3, 2014-08-06).

Although a secondary maximum of $N_{\rm H} = 3.6 \times 10^{23}$ cm^{-2} was seen 85 days after the start of the X-ray minimum in 2003 (Hamaguchi et al. 2007a), no such column density maximum was seen in the *Swift* data in 2014. Simulations (e.g., Madura et al. 2012) show that, at this orbital phase, the wind–wind collision between the two stars starts to "break out" of the inner wind of η Car-A, and we could reasonably expect that this should be a time when the X-ray column densities are especially sensitive to the density profile of the inner wind of η Car-A. We suggest that this column density difference may be due to a transient density inhomogeneity seen in the inner wind of η Car-A in 2003 that was not observed in 2014.

Attempts to model the variation in column density with phase analytically (Kashi & Soker 2009b) and numerically (Parkin et al. 2009, 2011) generally show large increases near periastron passage. In addition to the stellar wind parameters, calculated column densities depend sensitively on the assumed orbital elements (the argument of periastron, inclination, and eccentricity), and near the X-ray minimum, also on the amount of assumed soft X-ray contamination. The column densities calculated analytically by Kashi & Soker (2009b), and shown in their Figure 3, are similar to the column densities near periastron passage reported in Table 5 of Hamaguchi et al. (2007a), but this analytic model assumes an orientation in which η Car-B is in front of η Car-A at periastron passage. There's strong evidence arguing that η Car-B is behind η Car-A at the periastron passage (see, for example, Madura et al. 2012, and references therein). Numerical studies have also shown that the distortion of the wind of η Car-A caused by the motion of η Car-B near periastron passage (when the orbital speed of η Car-B is comparable to velocity of η Car-A's wind) also plays an important role in determining the overall

absorption along the line of sight to the extended X-ray emitting region.

5. Conclusions

We present X-ray fluxes, HRs, and column densities for η Car around the 2014 X-ray minimum, as observed by the *Swift* XRT in WT mode, and compare them to earlier data obtained by *RXTE* and other X-ray observatories. These data show the following.

1. The X-ray flux minimum began near 2014 August 01, consistent with the ephemeris given in Corcoran (2005), though the X-ray hardness variation suggests that the deep minimum may have begun two days earlier, on 2014 July 30. The *Swift* fluxes and X-ray HRs show that the onset of the X-ray minimum is reproducible (to within two days) over the past 18 years.
2. Analysis of the four X-ray minima allowed us to refine the X-ray period, $P = 2023.40 \pm 0.71$ days, which agrees very well with the period derived from analysis of the variations in the equivalent width of the He II line, 2022.7 ± 0.3 days (Teodoro et al. 2016), and the period derived by Damineli et al. (2008b), 2022.7 ± 1.3 days, using many different spectral lines and broad-band fluxes. This shows that the X-ray, optical, and He II variations are closely connected with stable periods.
3. Prior to the start of the X-ray minimum, the X-ray flux showed variability ("flaring") similar to that seen by *RXTE* in the previous three cycles. There is no consistent change in spectral color or HR during the flare episodes. Moffat & Corcoran (2009) showed that, at least for some flares observed in previous cycles, flare peak emission seemed to be associated with an increase in X-ray hardness, since the emission at $E > 3$ keV seemed to increase while the emission below 3 keV did not. The HR definition we use here is not sensitive to any such color change, since the lowest energy channel we consider is 3.5 keV.
4. The X-ray flux maximum observed by *Swift* was $3.71 \pm 0.93 \times 10^{-10}$ erg s^{-1} cm^{-2}, reached on 2014 July 12; this was larger than any previous flux measure from either *RXTE* or *Swift*. However, the flux derived from this observation has a higher uncertainty, since the source was unfortunately placed near a bad detector column. Observations with *MAXI* on 2014 June 17 yielded a flux 1.5 times higher than the *Swift* maximum (Negoro et al. 2014), but contemporaneous observations with *Swift* on 2014 June 14 and 2014 June 18 showed substantially lower X-ray flux levels, 2.62 ± 0.07 and $3.18 \pm 0.1 \times 10^{-10}$ erg s^{-1} cm^{-2}, respectively, which suggests either that the *MAXI* observation was obtained near the peak of an unusually bright and short-lived X-ray flare, or that the reported *MAXI* flux is overestimated. Nevertheless, the maximum X-ray flux seen in 2014 indicates either that, in the interval prior to the X-ray minimum, η Car has been growing brighter in X-rays, or that the pre-minimum X-ray flares are increasing in amplitude.
5. The *Swift* X-ray HR curve shows a rather smooth and symmetric rise and fall near the X-ray minimum. This improves on the *RXTE* HR variations near the X-ray minimum (Corcoran et al. 2010), which were significantly affected by the lower soft X-ray sensitivity and the higher low-energy X-ray background in the *RXTE*-PCA, a much better measure of the actual hardness variation. The *Swift* XRT show that the observed hardness peak occurred 40.5 days after the start of the X-ray minimum, and near a peak in the He II λ4686 emission line strength.
6. Overall, there is reasonably good agreement between the derived *Swift* column densities and those derived from analysis of previous *XMM*, *CHANDRA*, and *Suzaku* spectra, even at phases close to periastron passage. Significant differences in derived column density are seen, however: the maximum column density derived from the *Suzaku* spectrum during the deep minimum in 2009 is about a factor of 10 larger than the maximum column derived from analysis of other X-ray spectra; a *Suzaku* observation about 50 days before the start of the X-ray minimum in 2009 is also about a factor of 10 larger than the *Swift* data at a similar time prior to the 2014 X-ray minimum; and a secondary maximum seen 85 days after the start of the 2003 X-ray minimum was not apparent in the *Swift* columns observed 85 days after the start of the 2014 minimum. These differences probably indicate the presence of transient density inhomogeneties in the wind of η Car-A.
7. Inferior conjunction of η Car-A probably occurred near the phase of the maximum column density, $N_{\rm H} \approx 10^{25}$ cm^{-2} at $\Delta\ \phi = +0.009$, as derived by Hamaguchi et al. (2014a), sometime during the "Deep Minimum" phase interval. We suggest that inferior conjunction of η Car-A occurred close to the midpoint of the "Deep Minimum" in 2014, MJD 56875.3 (2014-08-06).
8. Six months before and after the X-ray minimum, the X-ray column derived from analysis of the *Swift* spectra was $\approx 5 \times 10^{22}$ cm^{-2}, nearly identical to the columns derived from analysis of *XMM* and *CHANDRA* spectra in 2003 by Hamaguchi et al. (2007a) at these X-ray phases. This probably represents the amount of absorbing material from the Homunculus Nebula along the line of sight to the X-ray emitting region, with some contribution by the wind of η Car-A (and the interstellar medium). The similarity of the columns measured outside the minima in 2003 and 2014 suggests that expansion of the Homunculus nebula over this interval does not play a significant role in determining the column to the X-ray source, and also suggests that any absorption by the wind of η Car-A (or η Car-B) at this phase is relatively constant.

Despite significant variations elsewhere in the X-ray cycle, the decline to the X-ray minimum state remains very regular over the four cycles studied by *RXTE* and *Swift*, and the start of the Deep X-Ray Minimum occurred within two days of the time predicted using the ephemeris of Corcoran (2005). The period derived from the X-ray data also remains in good agreement with periods derived from observations in other wavebands at lower energies. This is astoundingly regular for an extremely variable, unstable system like η Car. The cause of the changes observed prior to the ingress to, and during the egress from, the X-ray minimum state, however, is still unclear.

Simple analysis shows that variations in the primary's wind might account for the observed "rapid recovery" in 2009 (Kashi & Soker 2009a; Corcoran et al. 2010), requiring, for example, a factor of a few drop in η Car-A's mass-loss rate. But a change as large as this should also cause the integrated flux of the Hα, Hβ, Hδ, and Hγ emission lines to decrease by a factor of 2–3 (as noted by Madura et al. 2013), with similar changes to other optical emission lines. Mehner et al. (2010b, 2012, 2015) reported significant weakening of wind lines and Hα and Fe II in the 2009–2014 interval, along with a decrease in the strength of other prominent emission lines, but Teodoro et al. (2012b) reported no strong changes at Hδ in spectra obtained in the 1994–2010 interval. Nevertheless, it seems clear that the variation of the egress indicates some change in the wind of η Car-A and/or η Car-B. Futhermore, the similarity of the derived X-ray column densities from 2007 and 2014, at phases away from X-ray minimum, does not suggest any large change in wind absorption. The *Swift* observations of the 2014 recovery, intermediate between the 2009 and 2003 recoveries, suggest that whatever was responsible for the abrupt recovery of 2009 is not continuing. It is perhaps interesting to contrast the variation in the recovery from the X-ray minimum with the relative stability of the observed ingress to minimum. Perhaps this suggests that whatever caused the variation in the recovery may be triggered by periastron passage, perhaps a transition from stable adiabatic cooling to unstable radiative cooling, and back again.

M.F.C. gratefully acknowledges the allocation of the *Swift* director's discretionary time, without which key changes in the X-ray spectrum would have gone unseen. We sorrowfully note the passing of Dr. Neil Gehrels, the Principal Investigator and Director of the *Swift* Mission for NASA. This work would not have been successful without Dr. Gehrels's leadership of *Swift*, his scientific curiosity, and his boundless passion to explore new phenomena. We humbly dedicate this paper in his memory. M.F.C. and J.L. gratefully acknowledge support from NASA grant NNX15AB92G. M. F.C. acknowledges support from NASA under cooperative agreement number NNG06EO90A. T.I.M. and C.M.P.R. were supported by an appointment to the NASA Postdoctoral Program at the Goddard Space Flight Center, formerly administered by Oak Ridge Associated Universities, and subsequently by the Universities Space Research Association, through a contract with NASA. A.F.J.M. is grateful for financial aid from NSERC (Canada) and FQRNT (Québec). N.D.R. acknowledges postdoctoral support by the University of Toledo and by the Helen Luedtke Brooks Endowed Professorship. K.H. is supported by the *Chandra* grant GO4-15019A, the XMM-Newton grant NNX15AK62G, NNX16AN87G, and the ADAP grant NNX15AM96G. This research has made use of NASA's Astrophysics Data System. This research has made use of data and/or software provided by the High Energy Astrophysics Science Archive Research Center (HEASARC), which is a service of the Astrophysics Science Division at NASA/GSFC and the High Energy Astrophysics Division of the Smithsonian Astrophysical Observatory. This research made use of Astropy, a community-developed core Python package for Astronomy (Astropy Collaboration et al. 2013). This research also made use of PythonTex, developed and maintained by Geoffrey Poore (Poore 2015).

Facilities: *RXTE*(PCA), Swift(XRT), CXO(ACIS), Suzaku (XIS), XMM-Newton(EPIC).

Software: Astrophysical Plasma Emission Code (Smith et al. 2001; Foster et al. 2012), Astropy (Astropy Collaboration et al. 2013), Saoimage/DS9 (Joye & Mandel 2005), pcabackest (Blackburn 1995), pcarsp (Blackburn 1995), PIMMS (Mukai 1993), PythonTex (Poore 2015), XSPEC v12.8+ (Dorman & Arnaud 2001), XSELECT, and xrtpipeline (distributed as part of the HEASoft/FTOOLS software, Blackburn 1995).

References

Astropy Collaboration, Robitaille, T. P., Tollerud, E. J., et al. 2013, A&A, 558, A33
Blackburn, J. K. 1995, in ASP Conf. Ser. 77, Astronomical Data Analysis Software and Systems IV, ed. R. A. Shaw, H. E. Payne, & J. J. E. Hayes (San Francisco, CA: ASP), 367
Bradt, H. V., Rothschild, R. E., & Swank, J. H. 1993, A&AS, 97, 355
Burrows, D. N., Hill, J. E., Nousek, J. A., et al. 2005, SSRv, 120, 165
Corcoran, M. F. 2005, AJ, 129, 2018
Corcoran, M. F. 2012, in ASP Conf. Ser. 465, Proc. Scientific Meeting in Honor of Anthony F. J. Moffat, ed. L. Drissen et al. (San Francisco, CA: ASP), 330
Corcoran, M. F., Fredericks, A. C., Petre, R., Swank, J. H., & Drake, S. A. 2000, ApJ, 545, 420
Corcoran, M. F., Hamaguchi, K., Pittard, J. M., et al. 2010, ApJ, 725, 1528
Corcoran, M. F., & Ishibashi, K. 2012, in Astrophysics and Space Science Library 384, Eta Carinae and the Supernova Impostors, ed. K. Davidson & R. M. Humphreys (New York: Springer), 195
Corcoran, M. F., Ishibashi, K., Davidson, K., et al. 1997, Natur, 390, 587
Corcoran, M. F., Ishibashi, K., Swank, J. H., & Petre, R. 2001, ApJ, 547, 1034
Corcoran, M. F., Pollock, A. M. T., Hamaguchi, K., & Russell, C. 2011, arXiv:1101.1422
Damineli, A., Hillier, D. J., Corcoran, M. F., et al. 2008a, MNRAS, 386, 2330
Damineli, A., Hillier, D. J., Corcoran, M. F., et al. 2008b, MNRAS, 384, 1649
Davidson, K. 1971, MNRAS, 154, 415
Davidson, K., Gull, T. R., Humphreys, R. M., et al. 1999, AJ, 118, 1777
Davidson, K., & Humphreys, R. M. 1997, ARA&A, 35, 1
Davidson, K., Mehner, A., Humphreys, R. M., Martin, J. C., & Ishibashi, K. 2015a, ApJL, 801, L15
Davidson, K., Mehner, A., Humphreys, R. M., Martin, J. C., & Ishibashi, K. 2015b, ApJL, 801, L15
Dorman, B., & Arnaud, K. A. 2001, in ASP Conf. Ser. 238, Astronomical Data Analysis Software and Systems X, ed. F. R. Harnden, Jr., F. A. Primini, & H. E. Payne (San Francisco, CA: ASP), 415
Fahed, R., Moffat, A. F. J., Zorec, J., et al. 2011, MNRAS, 418, 2
Fernández-Lajús, E., Fariña, C., Torres, A. F., et al. 2009, A&A, 493, 1093
Foster, A. R., Ji, L., Smith, R. K., & Brickhouse, N. S. 2012, ApJ, 756, 128
Gaviola, E. 1950, ApJ, 111, 408
Gehrels, N., Chincarini, G., Giommi, P., et al. 2004, ApJ, 611, 1005
Groh, J. H., Hillier, D. J., Madura, T. I., & Weigelt, G. 2012a, MNRAS, 423, 1623
Groh, J. H., Madura, T. I., Hillier, D. J., Kruip, C. J. H., & Weigelt, G. 2012b, ApJL, 759, L2
Gull, T. R., Madura, T. I., Teodoro, M., et al. 2016, MNRAS, 462, 3196
Hamaguchi, K., Corcoran, M. F., Gull, T., et al. 2007a, ApJ, 663, 522
Hamaguchi, K., Corcoran, M. F., Gull, T. R., et al. 2016, ApJ, 817, 23
Hamaguchi, K., Corcoran, M. F., Russell, C. M. P., et al. 2014a, ApJ, 784, 125
Hamaguchi, K., Corcoran, M. F., Takahashi, H., et al. 2014b, ApJ, 795, 119
Hamaguchi, K., Petre, R., Matsumoto, H., et al. 2007b, PASJ, 59, 151
Herschel, J. F. W., Sir 1838, MNRAS, 4, 121
Hillier, D. J., Davidson, K., Ishibashi, K., & Gull, T. 2001, ApJ, 553, 837
Humphreys, R. M., & Davidson, K. 1994, PASP, 106, 1025
Humphreys, R. M., & Martin, J. C. 2012, in Astrophysics and Space Science Library 384 Eta Carinae and the Supernova Impostors, ed. K. Davidson & R. M. Humphreys (New York: Springer), 1
Ishibashi, K., Corcoran, M. F., Davidson, K., et al. 1999, ApJ, 524, 983
Joye, W. A., & Mandel, E. 2005, in ASP Conf. Ser. 347, Astronomical Data Analysis Software and Systems XIV, ed. P. Shopbell, M. Britton, & R. Ebert (San Francisco, CA: ASP), 110

Kashi, A., & Soker, N. 2009a, ApJL, 701, L59
Kashi, A., & Soker, N. 2009b, MNRAS, 397, 1426
Madura, T. I., Gull, T. R., Okazaki, A. T., et al. 2013, MNRAS, 436, 3820
Madura, T. I., Gull, T. R., Owocki, S. P., et al. 2012, MNRAS, 420, 2064
Martin, J. C., Davidson, K., Humphreys, R. M., Hillier, D. J., & Ishibashi, K. 2006a, ApJ, 640, 474
Martin, J. C., Davidson, K., & Koppelman, M. D. 2006b, AJ, 132, 2717
Mehner, A., Davidson, K., Ferland, G. J., & Humphreys, R. M. 2010a, ApJ, 710, 729
Mehner, A., Davidson, K., Humphreys, R. M., et al. 2010b, ApJL, 717, L22
Mehner, A., Davidson, K., Humphreys, R. M., et al. 2012, ApJ, 751, 73
Mehner, A., Davidson, K., Humphreys, R. M., et al. 2015, A&A, 578, A122
Moffat, A. F. J., & Corcoran, M. F. 2009, ApJ, 707, 693
Monnier, J. D., Zhao, M., Pedretti, E., et al. 2011, ApJL, 742, L1
Morris, P. W. 2015, arXiv:1510.08541
Morris, P. W., Waters, L. B. F. M., Barlow, M. J., et al. 1999, Natur, 402, 502
Mukai, K. 1993, PIMMS and Viewing: proposal preparation tools
Negoro, H., Fukushima, K., Mihara, T., et al. 2014, ATel, 6289, 1
Ostriker, J. P., & Gunn, J. E. 1971, ApJL, 164, L95
Parkin, E. R., Pittard, J. M., Corcoran, M. F., & Hamaguchi, K. 2011, ApJ, 726, 105
Parkin, E. R., Pittard, J. M., Corcoran, M. F., Hamaguchi, K., & Stevens, I. R. 2009, MNRAS, 394, 1758
Pian, E., Campana, S., Chincarini, G., et al. 2009, arXiv:0908.2819
Pittard, J. M., & Corcoran, M. F. 2002, A&A, 383, 636
Plavchan, P., Jura, M., Kirkpatrick, J. D., Cutri, R. M., & Gallagher, S. C. 2008, ApJS, 175, 191
Poore, G. M. 2015, CS&D, 8, 014010
Richardson, N. D., Madura, T. I., St-Jean, L., et al. 2016, MNRAS, 461, 2540
Smith, N. 2013, MNRAS, 429, 2366
Smith, N., Gehrz, R. D., Hinz, P. M., et al. 2003, AJ, 125, 1458
Smith, N., & Owocki, S. P. 2006, ApJL, 645, L45
Smith, R. K., Brickhouse, N. S., Liedahl, D. A., & Raymond, J. C. 2001, ApJL, 556, L91
Soker, N., & Behar, E. 2006, ApJ, 652, 1563
Soker, N., & Kashi, A. 2012, NewA, 17, 616
Steffen, W., Teodoro, M., Madura, T. I., et al. 2014, MNRAS, 442, 3316
Steiner, J. E., & Damineli, A. 2004, ApJL, 612, L133
Stellingwerf, R. F. 1978, ApJ, 224, 953
Teodoro, M., Damineli, A., Arias, J. I., et al. 2012a, ApJ, 746, 73
Teodoro, M., Damineli, A., Arias, J. I., et al. 2012b, ApJ, 746, 73
Teodoro, M., Damineli, A., Heathcote, B., et al. 2016, ApJ, 819, 131
Teodoro, M., Madura, T. I., Gull, T. R., Corcoran, M. F., & Hamaguchi, K. 2013, ApJL, 773, L16
Townsley, L. K., Broos, P. S., Chu, Y.-H., et al. 2011, ApJS, 194, 15
Verner, E., Bruhweiler, F., & Gull, T. 2005, ApJ, 624, 973
Westphal, J. A., & Neugebauer, G. 1969, ApJL, 156, L45
Williams, P. M., van der Hucht, K. A., Pollock, A. M. T., et al. 1990, MNRAS, 243, 662